

Efficient two-dimensional atom localization in a five-level conductive chiral atomic medium via birefringence beam absorption spectrum

Sajid Ali¹, Muhammad Idrees^{2,3,*}, Bakht Amin Bacha^{2,*}, Arif Ullah² and Muhammad Haneef¹

¹Lab of Theoretical Physics, Department of Physics, Hazara University, Mansehra 21300, Pakistan

²Quantum Optics and Quantum Information Research Group, Department of Physics, University of Malakand, Chakdara Dir(L), Khyber Pakhtunkhwa, Pakistan

³Zhejiang Province Key Laboratory of Quantum Technology and Device, Department of Physics, Zhejiang University, Hangzhou 310027, China

E-mail: aminoptics@gmail.com, idreesoptics@yahoo.com and idrees@zju.edu.cn

Received 12 July 2020, revised 21 October 2020

Accepted for publication 26 October 2020

Published 22 December 2020



Abstract

We have theoretically investigated two-dimensional atom localization using the absorption spectra of birefringence beams of light in a single wavelength domain. The atom localization is controlled and modified through tunneling effect in a conductive chiral atomic medium with absorption spectra of birefringent beams. The significant localization peaks are investigated in the left and right circularly polarized beam. Single and double localized peaks are observed in different quadrants with minimum uncertainty and significant probability. The localized probability is modified by controlling birefringence and tunneling conditions. These results may be useful for the capability of optical microscopy and atom imaging.

Keywords: 2D atom localization, birefringence beam absorption, chiral atomic medium

(Some figures may appear in colour only in the online journal)

1. Introduction

During the past few decades, atom localization has attracted attention on both theoretical and experimental fronts, primarily due to its wide scope in atom nanolithography [1, 2], trapping and cooling of neutral atoms [3], moving atoms center-of-mass wave function measurement [4, 5], Bose–Einstein condensation [6, 7], matter waves coherent patterning [8], etc. Various kinds of methods have evolved over the course of its progress. While the initial techniques included phase measurement of standing-wave fields [9, 10], atomic dipole, atomic fluorescence, dark resonance interference, spontaneous emission spectrum, and Raman gain process

measurement [11–17], they differ from modern ones. One such example is an atom, whose energy levels are placed under the influence of the standing wave fields in a sub-wavelength domain. This new technique has enabled us to witness some basic phenomena, which among many include electromagnetically induced absorption [18, 19], population trapping [20, 21], superluminal and subluminal propagation of light [22–26], Kerr nonlinearity [27, 28], optical bistability [29, 30], four-wave mixing [31, 32], electromagnetically induced transparency [33, 34] and optical multistability [35, 36]. Atom localization phenomena are also investigated by calculating the optical Bloch equations based on the formalism of the density matrix. It turns out that imaginary and real parts of the coherence term are directly related to the probe absorption and dispersion spectrum, respectively.

* Authors to whom any correspondence should be addressed.

Furthermore, highly efficient and high-resolution atomic localization in the subwavelength region is also observed via level population and probe absorption [37–47].

Recently, different schemes have been used for one-dimensional (1D) atom localization in subwavelength space through excited level population measurements [48–52], and probe field absorption spectra [53–57]. In such cases, the standing wave fields are applied along a single direction (i.e., x -axis) and the atom is localized in the 1D subwavelength space. Many new advanced (high-resolution and high-precision) proposals have emerged recently for two-dimensional (2D) and three-dimensional (3D) atom localization. 2D atom localization is experimentally realized by superimposing two standing wave fields. In 2010, Ivanov *et al* proposed a tripod four-level atomic scheme for 2D atom localization via excited-state population [41]. Ding and his coworkers, in 2011, introduced a four-level closed-loop system and observed 2D atom localization using the probe absorption measurement and the localization was done in a quadrant subwavelength space [38]. Hamedi *et al* proposed a five-level atomic scheme for the phase sensitive 2D atom localization via excited-state population [37]. A myriad of other proposals for the 2D atomic localization have appeared, as discussed in [58–62].

When linear polarized light passes through a chiral medium it splits into the left (LCP) and right circularly polarized (RCP) beams. The LCP and RCP beams have a slight difference in refractive indices ($n_r^{(+)}$, $n_r^{(-)}$). The difference in refractive indices ($\delta n = n_r^{(+)} - n_r^{(-)}$) is known as circular birefringence [63–65]. The circular birefringence and chiral medium affects the properties of light–matter interaction [66–68]. On a thorough literature survey, it appears no analysis has been carried out for atom localization by the birefringence absorption spectrum using the tunneling effect and conductive chiral medium. Inspired from the above studies, we here introduce a new way to localize atoms in the 2D space using dynamic conductive chiral atomic medium under the effects of quantum tunneling. The information of localization can be extracted by the birefringence absorption spectrum in one wavelength domain. The significant localization peaks are investigated in the LCP and RCP beams' absorption spectra. Single and double localized peaks in different quadrants with minimum uncertainty and significant probability are observed.

2. Model of the atomic system

A five-level atomic configuration is under consideration for the proposed aims and objectives, as shown in figure 1. Two electric probe fields E_p , that differ by phase φ_p , are driving between the states $|5, 3, 4\rangle$. The Rabi frequency of these probes is Ω_p and common detuning Δ_p . Two magnetic probe fields B_m , differing by phase φ_m , are driving between the states $|1, 2, 5\rangle$. The Rabi frequency of these probes is Ω_m and common detuning Δ_m . A control field E_1 is driving between

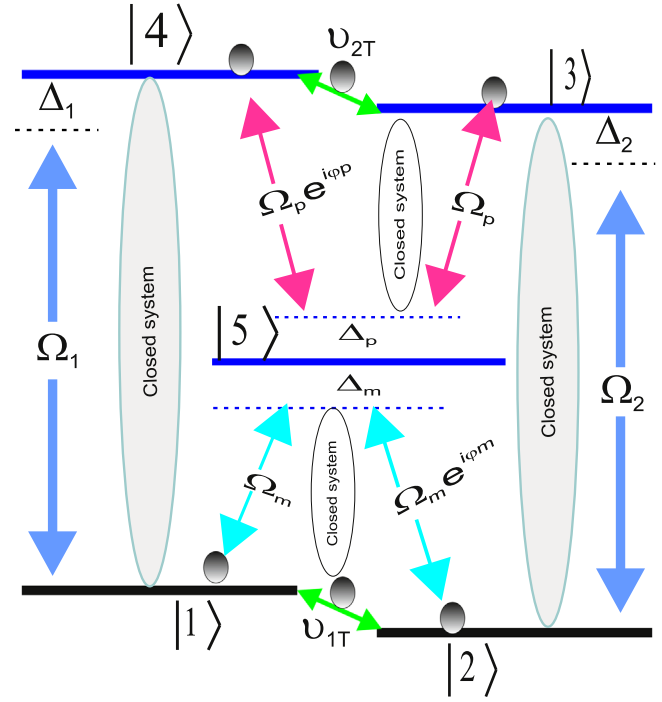


Figure 1. Schematic of five-level atomic configuration for the 2D atom localization through dynamic conductive chiral medium under the effects of quantum tunneling using birefringence absorption spectrum in one wavelength domain.

the states $|1, 4\rangle$. The Rabi frequency of the field is Ω_1 and its detuning Δ_1 . Another control field E_2 is driving between the states $|2, 3\rangle$. The Rabi frequency of the field is Ω_2 and its detuning Δ_2 . The excited states' spontaneous decay rates are γ_{32} , γ_{35} , γ_{41} , γ_{45} , γ_{51} , and γ_{52} . The system is closed between the states $|1, 4, 5\rangle$ and $|2, 3, 5\rangle$ by control and electric/magnetic fields. The levels $|3, 4\rangle$ and $|1, 2\rangle$ are so close to each other that atomic kinetic energy $p^2/2m$ obeys the uncertainty principle $\Delta p \cdot \Delta x \geq \hbar$ and $\Delta E \cdot \Delta t \geq \hbar$. The tunneling between two states $|3, 4\rangle$ and $|1, 2\rangle$ are possible when Δx is larger than the states' separation ΔL . Under these circumstances, an atom tunnels between the levels $|3, 4\rangle$ and $|1, 2\rangle$ with frequencies ν_{1T} and ν_{2T} .

The position dependent tunneling frequencies are written as [58–61] $\nu_{1T}(x, y) = T[\sin(\eta_1 kx) + \sin(\eta_2 ky + \varphi_3)]$ and $\nu_{2T}(x, y) = T[\sin(\eta_3 kx) + \sin(\eta_5 ky + \varphi_4)]$. The parameter T represents the space independent parts of tunneling frequencies and φ_3 , φ_4 its phases. Wave vectors associated with the standing-waves respectively are $k_i = k\eta_i$ ($i = 1, 2, 3, 5$). The interaction Hamiltonian for the system is written as:

$$H_I = -\frac{\hbar}{2} [\Omega_m e^{-i\Delta_m t} |1\rangle\langle 5| + \Omega_m e^{-i\varphi_m} e^{-i\Delta_m t} |2\rangle\langle 5| + \Omega_p e^{-i\varphi_p} e^{-i\Delta_p t} |5\rangle\langle 4| + \Omega_p e^{-i\Delta_p t} |5\rangle\langle 3| + \Omega_1 e^{-i\Delta_1 t} |1\rangle\langle 4| + \Omega_2 e^{-i\Delta_2 t} |2\rangle\langle 3| + \hbar[\nu_{1T}(x, y)|1\rangle\langle 2| + \nu_{2T}(x, y)|4\rangle\langle 3|] + \text{H.C.}] \quad (1)$$

The detunings of these fields are related to their corresponding angular frequencies and atomic states' resonance frequencies as: $\Delta_1 = \omega_1 - \omega_{14}$, $\Delta_2 = \omega_2 - \omega_{23}$, $\Delta_p = \omega_p - \omega_{45,35}$ and $\Delta_m = \omega_m - \omega_{15,25}$. The master equation for the density matrix is given by [57, 69]

$$\dot{\rho} = -\frac{i}{\hbar}[H_I, \rho] - \frac{1}{2}\sum \gamma_{ij}(\delta^\dagger \delta \rho + \rho \delta^\dagger \delta - 2\delta \rho \delta^\dagger), \quad (2)$$

where H_I represents the interaction Hamiltonian of the system, γ_{ij} denotes the spontaneous decay rate from the excited state $|i\rangle$ to the ground state $|j\rangle$ (i.e., $\gamma_{41}, \gamma_{45}, \gamma_{32}, \gamma_{35}, \gamma_{51}, \gamma_{52}$) and δ^\dagger (δ) is the general raising (lowering) operator. Using $\rho_{ij} = \tilde{\rho}_{ij} \exp[-i\Delta_j t]$, $j = 1, 2, p, m$ in the dynamical equations of motion and after simplification, the following coupled rates equations are obtained.

$$\begin{aligned} \dot{\tilde{\rho}}_{35} = & A_1 \tilde{\rho}_{35} + \frac{i}{2}\Omega_p(\tilde{\rho}_{55} - \tilde{\rho}_{33}) + \frac{i}{2}\Omega_2 \tilde{\rho}_{25} - \frac{i}{2}\Omega_m \tilde{\rho}_{31} \\ & - \frac{i}{2}\Omega_m e^{i\varphi_m} \tilde{\rho}_{32} - \frac{i}{2}\Omega_p e^{-i\varphi_p} \tilde{\rho}_{34} - i\nu_{2T} \tilde{\rho}_{45}, \end{aligned} \quad (3)$$

$$\begin{aligned} \dot{\tilde{\rho}}_{45} = & A_1 \tilde{\rho}_{45} + \frac{i}{2}\Omega_p e^{-i\varphi_p}(\tilde{\rho}_{55} - \tilde{\rho}_{44}) + \frac{i}{2}\Omega_1 \tilde{\rho}_{15} \\ & - \frac{i}{2}\Omega_m e^{i\varphi_m} \tilde{\rho}_{42} - \frac{i}{2}\Omega_p \tilde{\rho}_{43} - i\nu_{2T} \tilde{\rho}_{35}, \end{aligned} \quad (4)$$

$$\begin{aligned} \dot{\tilde{\rho}}_{25} = & A_2 \tilde{\rho}_{25} + \frac{i}{2}\Omega_m e^{i\varphi_m}(\tilde{\rho}_{55} - \tilde{\rho}_{22}) + \frac{i}{2}\Omega_2 \tilde{\rho}_{35} \\ & - \frac{i}{2}\Omega_m \tilde{\rho}_{21} - \frac{i}{2}\Omega_p \tilde{\rho}_{23} - \frac{i}{2}\Omega_p e^{-i\varphi_p} \tilde{\rho}_{24} - i\nu_{1T} \tilde{\rho}_{15}, \end{aligned} \quad (5)$$

$$\begin{aligned} \dot{\tilde{\rho}}_{15} = & A_3 \tilde{\rho}_{15} + \frac{i}{2}\Omega_m \tilde{\rho}_{55} - \tilde{\rho}_{11} + \frac{i}{2}\Omega_1 \tilde{\rho}_{45} - \frac{i}{2}\Omega_m e^{-i\varphi_m} \tilde{\rho}_{12} \\ & - \frac{i}{2}\Omega_p \tilde{\rho}_{13} - \frac{i}{2}\Omega_p e^{-i\varphi_p} \tilde{\rho}_{14} - i\nu_{1T} \tilde{\rho}_{25}. \end{aligned} \quad (6)$$

The terms A_{1-3} are written in the [appendix](#). Applying the first order perturbation condition to the coupled rates equations, while taking $\Omega_{p,m}$ in the first order and $\Omega_{1,2}$ in all orders the atoms are prepared in the metastable state $|5\rangle$. The population in the other states are assumed to be null. This implies that its density element $\tilde{\rho}_{55}^{(0)} = 1$. Then the population in other states are zero such as $\tilde{\rho}_{22,33,44}^{(0)} = 0$ and $\tilde{\rho}_{42,43,21,23,12,13}^{(0)} = 0$. After application of the first order perturbation condition, the coupled density matrix equations $\tilde{\rho}_{35,45,25,15}$ are solved by considering the following integral [70]

$$L(t) = \int_{-\infty}^t e^{-G(t-t')} P dt = G^{-1}Y, \quad (7)$$

where $L(t)$ and Y are column matrices and G is a 4×4 matrix. For more details, we refer the reader to [55, 57]. The matrix form of this equation is written in the [appendix](#). The effective coherence terms $\tilde{\rho}_{35}^{(1)} + \tilde{\rho}_{45}^{(1)}$ and $\tilde{\rho}_{25}^{(1)} + \tilde{\rho}_{15}^{(1)}$ are related to electric effective polarization and magnetization, such as $P = Nd(\tilde{\rho}_{35}^{(1)} + \tilde{\rho}_{45}^{(1)})$ and $M = N\mu(\tilde{\rho}_{25}^{(1)} + \tilde{\rho}_{15}^{(1)})$. The effective electric and magnetic dipole moments between the states are respectively $\mu = \sqrt{\frac{3\hbar(\gamma_{51} + \gamma_{52})\lambda^3}{8\pi^2}}$ and $d = c\sqrt{\frac{3\hbar(\gamma_{51} + \gamma_{52})\lambda^3}{8\pi^2}}$.

Replacing $\Omega_p = E_p d/\hbar$ and $\Omega_m = B_m \mu/\hbar$ while $B_m = \mu_0(H + M)$ in the polarization and magnetization equations $P = Nd(\tilde{\rho}_{35}^{(1)} + \tilde{\rho}_{45}^{(1)})$ and $M = N\mu(\tilde{\rho}_{25}^{(1)} + \tilde{\rho}_{15}^{(1)})$, we get

$$P = \alpha_1 E_p + \alpha_2 H, M = \alpha_3 E_p + \alpha_4 H. \quad (8)$$

The terms α_{1-4} are given in the [appendix](#). The electric polarization and magnetization in terms of chiral coefficient and electric magnetic susceptibility are given in [28, 47]

$$P = \epsilon_0 \chi_e E_p + \frac{\xi_{E_p H}}{c} H, M = \frac{\xi_{H E_p}}{\mu_0 c} E_p + \chi_m H. \quad (9)$$

Comparing (8) and (9), we obtain the following chiral coefficients and electric and magnetic susceptibility

$$\chi_e = \frac{Nd^2}{\epsilon_0 \hbar} \left[\frac{\alpha_1(\hbar - N\mu^2 \mu_0 \alpha_4) + N\mu^2 \mu_0 \alpha_2 \alpha_3}{\hbar - N\mu^2 \mu_0 \alpha_4} \right], \quad (10)$$

$$\chi_m = \frac{N\mu^2 \mu_0 \alpha_4}{\hbar - N\mu^2 \mu_0 \alpha_4}, \quad (11)$$

$$\xi_{HE} = \frac{Nc\mu\mu_0\alpha_3 d}{\hbar - N\mu^2 \mu_0 \alpha_4}, \quad (12)$$

and

$$\xi_{EH} = \frac{Nc\mu\mu_0\alpha_2 d}{\hbar - N\mu^2 \mu_0 \alpha_4}, \quad (13)$$

where A_{1-4} and α_{1-4} are in the [appendix](#). The refractive indices of the LCP and RCP beams are written as (for more details see [28, 47])

$$\begin{aligned} n_r^{(\pm)} = & \sqrt{(1 + \chi_e)(1 + \chi_m) - \frac{(\xi_{EH} + \xi_{HE})^2}{4}} \pm \frac{i}{2}(\xi_{EH} - \xi_{HE}), \end{aligned} \quad (14)$$

where $n_r^{(+)}$ stands for the RCP beam complex refractive index and $n_r^{(-)}$ stands for the LCP beam complex refractive index. If $\xi_{EH(HE)} = 0$, then the medium is an ordinary refractive medium, when $\text{Re}(n_r^{(\pm)})$ is positive. The medium is negative refractive, when $\text{Re}(n_r^{(\pm)})$ is negative. However, if $\xi_{EH(HE)} \neq 0$, the medium is chiral. The chiral medium contributed additional terms of chiral coefficients to refractive indices along with relative permittivity $\epsilon_r = 1 + \chi_e$ and permeability $\mu_r = 1 + \chi_m$ terms. To find the dependence of the dielectric function dependent on conductivity, we use the following Maxwell equations for conductive medium

$$\nabla \cdot E = 0, \nabla \cdot B = 0, E = -\frac{\partial B}{\partial t}, \nabla \times B = \mu J + \mu \epsilon \frac{\partial E}{\partial t}, \quad (15)$$

where E and B are the electric and magnetic fields, respectively. ϵ represents the permittivity and μ represents the permeability of the material. By applying curl to (14), we get

$$\nabla^2 E = \mu \epsilon \frac{\partial E}{\partial t} + \mu \epsilon \frac{\partial^2 B}{\partial t^2}, \quad (16)$$

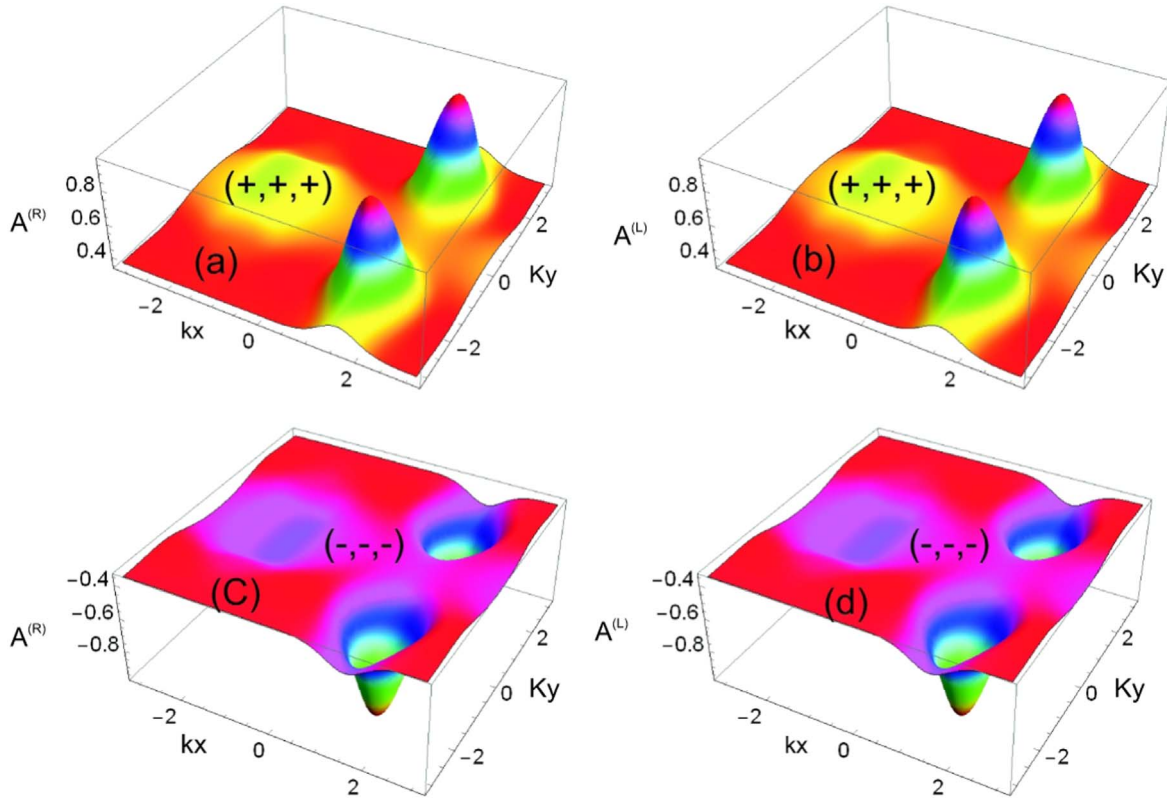


Figure 2. Birefringence absorption coefficients as functions of (kx, ky) . The parameters supposed here are $\gamma = 36.1$ GHz, $\gamma_{32,35,41,45} = 2\gamma$, $\gamma_{51,52} = 0.2\gamma$, $\Delta_p = 0.5\gamma$, $\Delta_1 = 0\gamma$, $\varphi_1 = \pi/4$, $\varphi_2 = \pi/3$, $\varphi_p = \pi/2$, $\varphi_m = 0$, $|\Omega_{1,2}| = 20\gamma$, $\sigma_{i,r} = 1000S/m$, $\eta_{1,3} = 1$, $\eta_{2,4} = -1$, $T = 10$, $\varphi_3 = 3\pi/2$, $\varphi_4 = \pi/2$ (+, +, +) birefringence condition for (a) and (b) while (-, -, -) birefringence condition for (c) and (d).

$$\nabla^2 B = \mu\epsilon \frac{\partial B}{\partial t} + \mu\epsilon \frac{\partial^2 B}{\partial t^2}. \quad (17)$$

The solution for the above equations are

$$E(r, t) = E_0 \exp(i(k \cdot r - \omega t)), \quad (18)$$

$$B(r, t) = B_0 \exp(i(k \cdot r - \omega t)), \quad (19)$$

where E_0 and B_0 are the complex amplitudes. For more details, see [57].

Equations (17) and (18) are the wave equations describing propagation of electromagnetic waves in the metal. Differentiating equation (17) twice and substituting in equation (15), we get

$$k_m^2 = \mu\epsilon\omega^2 + i\mu\sigma\omega, \quad (20)$$

$$k = k_{m1} + ik_{m2}, \quad \epsilon = \epsilon_r + i\epsilon_i, \quad \sigma = \sigma_r + i\sigma_i, \quad (21)$$

$$k_m^2 = (\mu\epsilon_r\omega^2 - \mu\sigma_i\omega) + i(\mu\epsilon_i\omega^2 + \mu\sigma_r\omega), \quad (22)$$

$$k_{m1}^2 - k_{m2}^2 = (\mu\epsilon_r\omega^2 - \mu\sigma_i\omega), \quad (23)$$

$$2k_{m1}k_{m2} = (\mu\epsilon_i\omega^2 + \mu\sigma_r\omega), \quad (24)$$

$$k = \pm \frac{\beta_1}{\sqrt{2}} \left[\sqrt{1 \pm \left(\frac{\beta_2}{\beta_1}\right)^4} + i\sqrt{-1 \pm \sqrt{1 + \left(\frac{\beta_2}{\beta_1}\right)^4}} \right], \quad (25)$$

where

$$\beta_1 = k_0 \sqrt{\epsilon' - \frac{\sigma_i}{\epsilon_0\omega}}, \quad \beta_2 = k_0 \sqrt{\epsilon'' + \frac{\sigma_r}{\epsilon_0\omega}}. \quad (26)$$

Real and imaginary parts of the permittivity in terms of the corresponding dielectric constants, $\epsilon_r = \epsilon_0\epsilon'$ and $\epsilon_i = \epsilon_0\epsilon''$, we have

$$k_{m1}^2 - k_{m2}^2 = \mu\epsilon_0\omega^2 \left(\epsilon' - \frac{\sigma_i}{\epsilon_0\omega} \right) = k_0^2 \left(\epsilon' - \frac{\sigma_i}{\epsilon_0\omega} \right) = \beta_1^2, \quad (27)$$

$$2k_{m1}k_{m2} = \mu\epsilon_0\omega^2 \left(\epsilon'' + \frac{\sigma_r}{\epsilon_0\omega} \right) = k_0^2 \left(\epsilon'' + \frac{\sigma_r}{\epsilon_0\omega} \right) = \beta_2^2, \quad (28)$$

where we used $\mu_0\epsilon_0 = 1/c$ and $k_0 = \omega/c$. Real and imaginary propagation parameters k_{m1} and k_{m2} are found by separating equations (23) and (24) we get

$$k^{(R,L)} = \pm k_0 \frac{\sqrt{\epsilon' - \frac{\sigma_i}{\epsilon_0\omega}}}{\sqrt{2}} \left[i\sqrt{-1 \pm \sqrt{1 + \frac{\left(\epsilon'' + \frac{\sigma_r}{\epsilon_0\omega}\right)^4}{\left(\epsilon' - \frac{\sigma_i}{\epsilon_0\omega}\right)^4}}} + \sqrt{1 \pm \sqrt{1 + \frac{\left(\epsilon'' + \frac{\sigma_r}{\epsilon_0\omega}\right)^4}{\left(\epsilon' - \frac{\sigma_i}{\epsilon_0\omega}\right)^4}}} \right]. \quad (29)$$

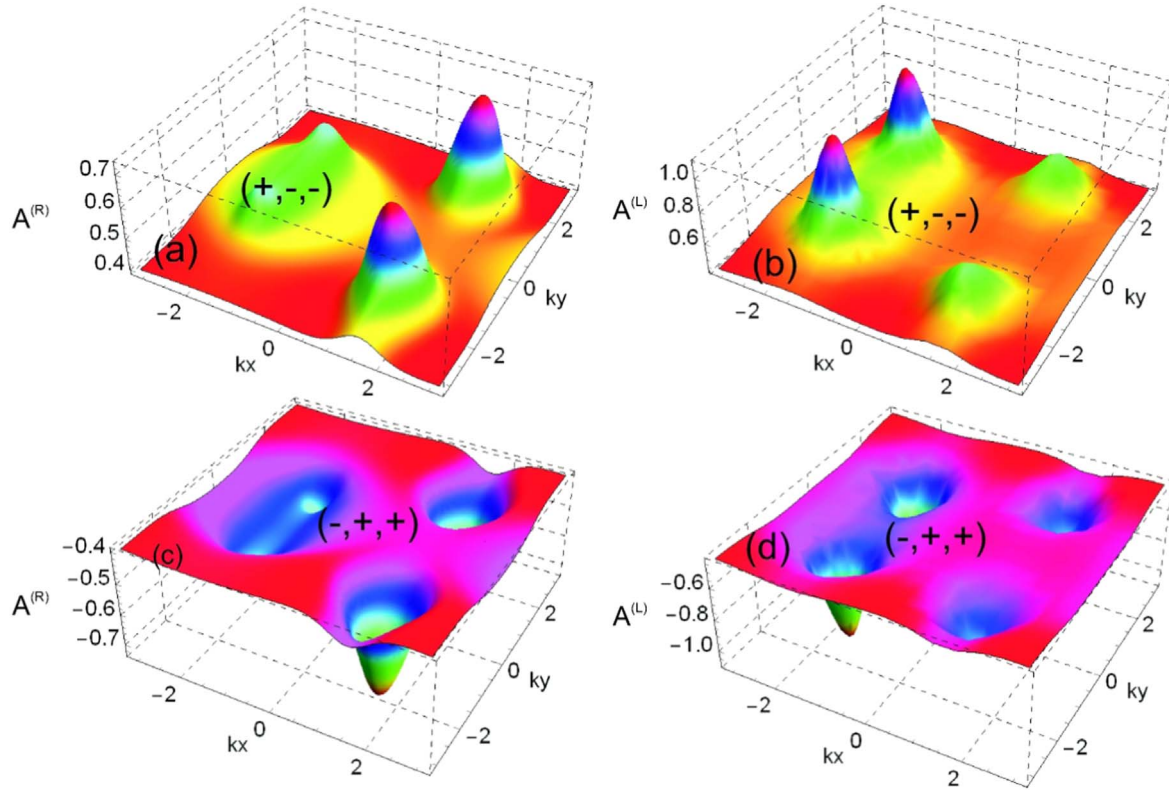


Figure 3. Birefringence absorption coefficients as functions of (kx, ky) . The parameters supposed here are $\gamma = 36.1$ GHz, $\gamma_{32,35,41,45} = 2\gamma$, $\gamma_{51,52} = 0.2\gamma$, $\Delta_p = 0.5\gamma$, $\Delta_1 = 0\gamma$, $\varphi_1 = \pi/4$, $\varphi_2 = \pi/3$, $\varphi_p = \pi/2$, $\varphi_m = 0$, $|\Omega_{1,2}| = 20\gamma$, $\sigma_{i,r} = 1000 \text{ S m}^{-1}$, $\eta_{1,3} = 1$, $\eta_{2,4} = -1$, $T = 10$, $\varphi_3 = 3\pi/2$, $\varphi_4 = \pi/2$ (+, -, -) birefringence condition for (a) and (b) while (-, +, +) birefringence condition for (c) and (d).

3. Results and discussion

The birefringence beams absorption coefficients through a dynamic conductive chiral medium are investigated under the effect of quantum tunneling for the atom localization. The decay rate of the atomic state is supposed to $\gamma = 36.1$ MHz. Here $|\Omega_{1,2}| = |\Omega_{1,2}| \exp(i\varphi_{1,2})$, $\omega_0 = 10^4\gamma$ and $\lambda = 2\pi c/\omega$. The other frequency parameters are scaled with γ . In the chiral atomic system, two probes of electric and magnetic fields are applied. The strong control fields are coupled in the system to modify the behavior of electric and magnetic probes. For the conductive chiral medium, we calculated 16 types of wave vectors for birefringence due to three \pm signs. This is related to 16 types of absorption coefficients and refractive indices. We have localized the atom by the birefringent beams for the cases of (+, +, +), (+, -, -), (-, +, +) and (-, -, -). The absorption coefficient is related to the imaginary part of the complex wave vector ($\text{Im}(k^{(R,L)}) = A^{(R,L)}$), while the real part of the complex wave vector is related to phase velocity and group velocity.

In figure 2, the plots are traced for atom localization through the dynamic conductive chiral medium under the effects of quantum tunneling using the birefringence absorption spectrum in one wavelength domain. Under the specific parametric condition, we have noticed two localized peaks in both the LCP and RCP light beams in inverse space of kx and

ky . For the case, (+, +, +) and (-, -, -) two localized peaks are investigated by LCP and RCP beams' absorption spectra. At the condition (+, +, +) two localized peaks are noted at the LCP and RCP beams absorption spectrum in the first and fourth quadrants in the 2D inverse position space. Here, one localized peak is in the first and another one is in the fourth quadrant. It means that we have two possible localized positions for an atom localization as shown in figures 2(a) and (b). At the condition (-, -, -) two localized peaks are noted at the LCP and RCP beams amplification (negative absorption) spectrum in the first and fourth quadrants in 2D inverse position space. It means the amplification occurs in the birefringent beams at the conditions of (-, -, -). At the birefringence beams amplifications, two downward localized peaks are investigated in the 2D plane (shown as figures 2(c) and (d)). It has been pointed out that these localized peaks also show two possible positions for the atom localization using birefringence absorption spectrum in a single wavelength domain.

In figure 3, the plots are traced for atom localization through dynamic conductive chiral medium under the effects of quantum tunneling using birefringence absorption/amplification spectra in one wavelength domain of 2D inverse space. The parametric condition for this figure is the same as given in figure 2, but we have changed only the birefringence condition from (+, +, +) and (-, -, -) to (+, -, -) and

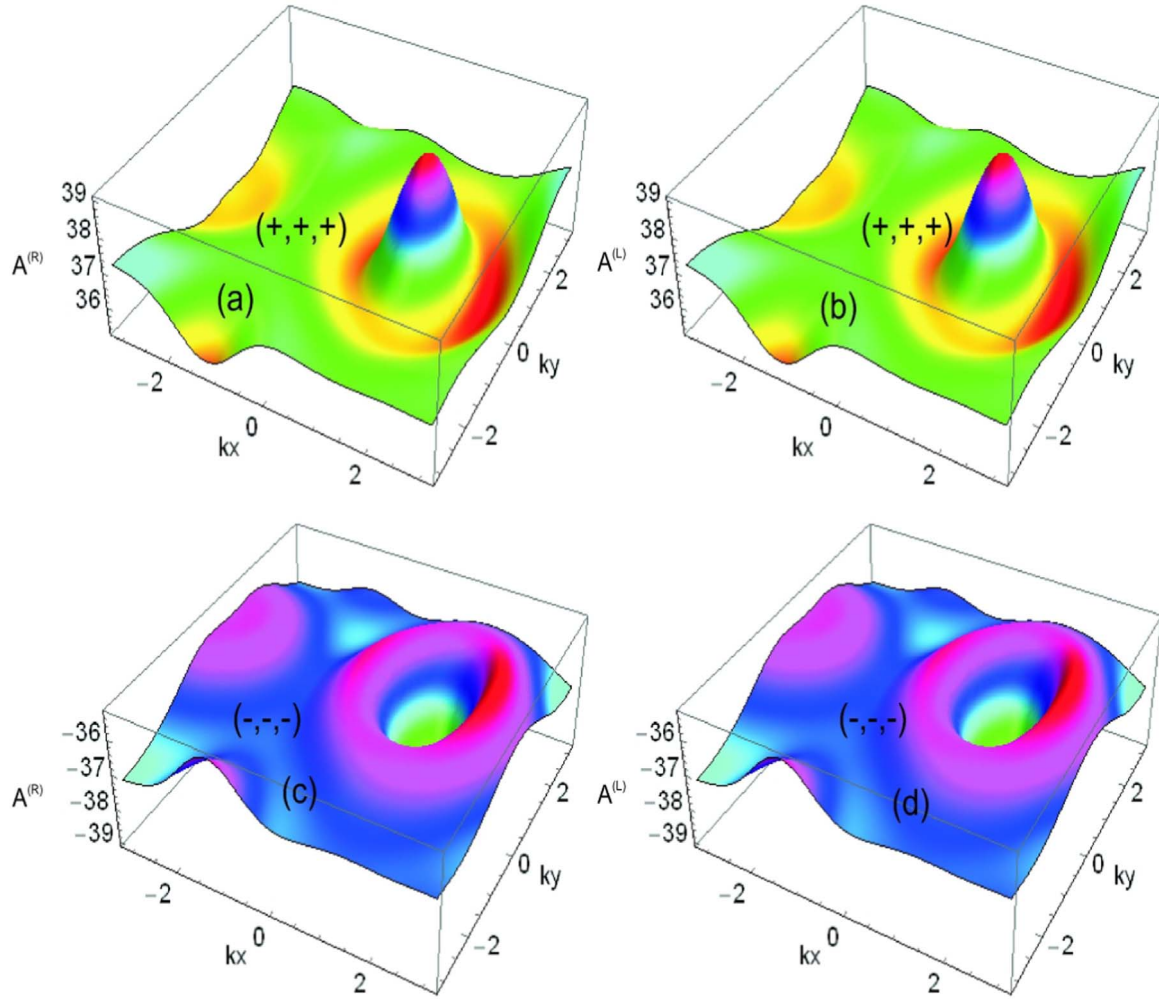


Figure 4. Birefringence absorption coefficients as functions of (k_x, k_y) . The parameters supposed here are $\gamma = 36.1$ GHz, $\gamma_{41} = 0.27\gamma$, $\gamma_{32} = 0.21\gamma$, $\gamma_{51} = 0.97\gamma$, $\gamma_{52} = 0.7\gamma$, $\gamma_{45} = 2.7\gamma$, $\gamma_{35} = 0.3\gamma$, $\Delta_p = 0.5\gamma$, $\Delta_1 = -1\gamma$, $\varphi_1 = \pi/2$, $\varphi_2 = \pi/3$, $\varphi_p = \pi/2$, $\varphi_m = \pi/4$, $|\Omega_1| = 15\gamma$, $|\Omega_2| = 10\gamma$, $\sigma_r = 10000$ S m $^{-1}$, $\sigma_i = 1500$ S m $^{-1}$, $\eta_1 = 1.35$, $\eta_2 = 0.5$, $\eta_3 = 0.2$, $\eta_4 = 0.8$, $T = 10$, $\varphi_3 = \pi/2$, $\varphi_4 = \pi/3$ $(+, +, +)$ birefringence condition for (a) and (b) while $(-, -, -)$ birefringence condition for (c) and (d).

$(-, +, +)$, respectively. Two large localized and two small localized peaks were reported by the absorption and amplification spectra of the RCP and LCP beams in the 2D inverse plane in one wavelength domain. At condition $(+, -, -)$, the RCP beam shows two small localized peaks in the second and third quadrants and two large localized peaks in the first and fourth quadrants. The localized peaks at the absorption spectrum of the LCP beam are the mirror images of localized peaks, which occur by the absorption spectrum of RCP beams as shown in figures 3(a) and (b). Further, two large localized and two small localized peaks were reported by the amplification spectra of the RCP and LCP beams in the 2D inverse plane in one wavelength domain. At condition $(-, +, +)$, the RCP beam shows two small localized peaks in the second and third quadrants and two large localized peaks in the first and fourth quadrants by its amplification spectra. The localized peaks at the amplification spectrum of the LCP beam are the mirror images of localized peaks that occur by the amplification spectrum of RCP beams as shown in figures 3(c) and (d).

To explicitly show the high resolution and high precision atomic localization through the birefringence absorption probe spectra, we modify the 2D atom localization behaviors as shown in figure 4. In figure 4, the plots are traced for atom localization through the dynamic conductive chiral medium under the effects of quantum tunneling using birefringence absorption/amplification spectra in one wavelength domain. The condition of $(+, +, +)$ the RCP and LCP beams' absorption spectra show a single broad localized peak in the first quadrant. It means that we have a single possible localized position for an atom as shown in figures 4(a) and (b). Furthermore, when we changed the birefringent condition to $(-, -, -)$, the downward localized peaks were investigated by RCP and LCP beam amplification spectra. In this figure, it is reported that the conditional position probability occurs at a specific point and is maximum there. The localized probability occurs at the LCP and RCP beams amplification spectra and are the mirror images of localized probability occurring at absorption spectra as shown in figures (c) and (d).

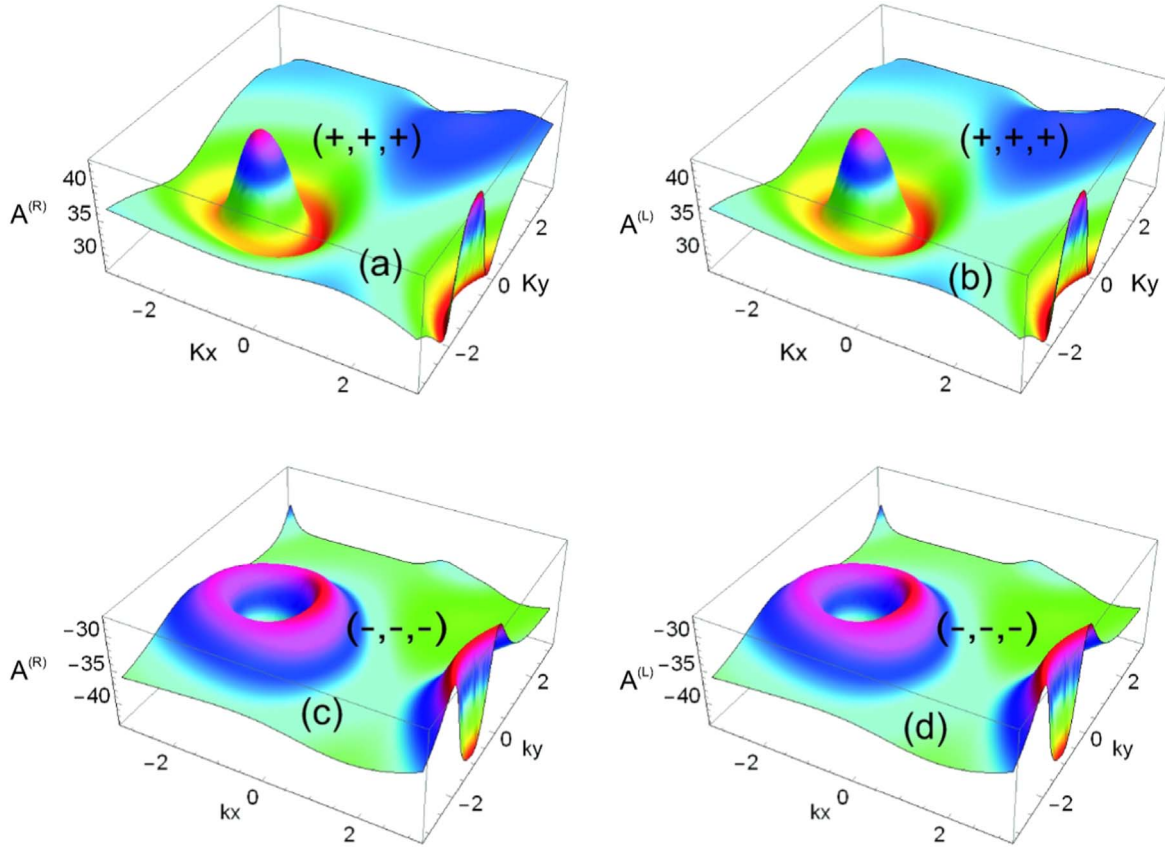


Figure 5. Birefringence absorption coefficients as functions of (kx, ky) . The parameters supposed here are $\gamma = 36.1$ GHz, $\gamma_{41,32,51,52,45,35} = 2.5\gamma$, $\Delta_p = 0.5$, $\Delta_1 = 0\gamma$, $\varphi_1 = \pi/4$, $\varphi_2 = \pi/3$, $\varphi_p = \pi/2$, $\varphi_m = 0$, $|\Omega_{1,2}| = 21\gamma$, $\sigma_{i,r} = 1000 \text{ S m}^{-1}$, $\eta_{1,3} = 1$, $\eta_{2,4} = -1$, $T = 10$, $\varphi_3 = 3\pi/2$, $\varphi_4 = \pi/2$ (+, +, +) birefringence condition for (a) and (b) while (-, -, -) birefringence condition for (c) and (d).

To modify the 2D atom microscopy for advanced high resolution and high precision, the birefringence absorption/amplification spectra are checked at another parametric condition. In figure 5, the plots are traced for atom localization through the dynamic conductive chiral medium under the effect of quantum tunneling using birefringence absorption/amplification spectra in one wavelength domain. The shift in the localized peaks are reported in the absorption and amplification spectra. We have investigated more interesting results such that the shift occurs in the localized peaks for other parametric conditions under same birefringence condition. The localized peak was investigated in the joint region of the second and third quadrants of the 2D space by the absorption/amplification spectra of the RCP and LCP beams under the conditions (+, +, +) and (-, -, -). It means that we have a single possible localized position for an atom in the joint region of the second and third quadrants. The localized peaks that occur at birefringent absorption spectra are the mirror images of the localized peaks that occur at birefringent amplification spectra, as depicted by figures 5(a)–(d).

4. Conclusion

In conclusion, a five-level chiral atomic medium (driven by two electric and magnetic probes with the two extra driving

control fields) are used to modify the birefringence under quantum tunneling conditions. Likewise, density matrix formalism and Maxwell's equation are also used to modify optical birefringence influenced by complex conductivity and tunneling effect. Moreover, 16 types of absorption coefficients are reported for conductive chiral atomic medium under the complex conductivity conditions. Therefore, the two-dimensional atom localization is investigated using the absorption spectrum of birefringence beams of light in a single wavelength domain. The localized peaks are studied for the conditions of (+, +, +), (+, -, -), (-, +, +) and (-, -, -) of the left and right circularly polarized beams absorption spectra. Two and a single localized peaks are reported in different quadrants with minimum uncertainty and significant probability. The localized probability is modified with the control of birefringence, tunneling and complex conductivity amplitude. These results may be useful for the capability of optical microscopy and atom imaging.

Appendix

The terms α_{1-4} occurring in equation (8) are written here. These terms are measured from coherence $\tilde{\rho}_{35}$, $\tilde{\rho}_{45}$, $\tilde{\rho}_{25}$ and $\tilde{\rho}_{15}$ using equation (7)

$$\alpha_1 = \frac{e^{-i(\varphi_1+\varphi_2+\varphi_p)}(Q_1 + 2ie^{i(2\varphi_1+\varphi_2)}(A_3|\Omega_2|^2 + 4A_1(\nu_{1T}^2 + A_2A_3) + 4iA_2A_3\nu_{2T} + 4i\nu_{1T}^2\nu_{2T} + e^{i\varphi_p}(A_2|\Omega_1|^2 + Q_2)))}{(4A_1A_3 + |\Omega_1|^2)|\Omega_2|^2 + 4A_1(A_2|\Omega_1|^2 + 4A_1(A_2A_3 + \nu_{1T}^2)) + 16(A_2A_3 + \nu_{1T}^2)\nu_{2T}^2 - 8|\Omega_1||\Omega_2|\nu_{1T}\nu_{2T}\cos(\varphi_1 - \varphi_2)},$$

$$\alpha_2 = \frac{e^{-i(\varphi_1+\varphi_2)}(4A_1|\Omega_1|e^{i\varphi_2}(A_2 + i\nu_{1T}e^{\varphi_m}) + |\Omega_1|e^{i\varphi_2}Q_3 + |\Omega_2|e^{i\varphi_1}(4i\nu_{1T}(A_1 + i\nu_{2T}) + e^{i\varphi_m}(4A_1A_3 + |\Omega_1|^2 + 4iA_3\nu_{2T})))}{(4A_1A_3 + |\Omega_1|^2)|\Omega_2|^2 + 4A_1(A_2|\Omega_1|^2 + 4A_1(A_2A_3 + \nu_{1T}^2)) + 16(A_2A_3 + \nu_{1T}^2)\nu_{2T}^2 - 8|\Omega_1||\Omega_2|\nu_{1T}\nu_{2T}\cos(\varphi_1 - \varphi_2)},$$

$$\alpha_3 = \frac{e^{-i\varphi_p}(|\Omega_2|e^{i\varphi_2}(e^{i\varphi_p}(|\Omega_1|^2 + 4A_1(A_3 + i\nu_{1T})) + 4i(A_3 + i\nu_{1T})\nu_{2T}) + e^{i\varphi_1}|\Omega_1|^2(|\Omega_2|^2 + 4(A_2 + i\nu_{1T})(A_1 + ie^{i\varphi_p}\nu_{2T})))}{(4A_1A_3 + |\Omega_1|^2)|\Omega_2|^2 + 4A_1(A_2|\Omega_1|^2 + 4A_1(A_2A_3 + \nu_{1T}^2)) + 16(A_2A_3 + \nu_{1T}^2)\nu_{2T}^2 - 8|\Omega_1||\Omega_2|\nu_{1T}\nu_{2T}\cos(\varphi_1 - \varphi_2)}$$

and

$$\alpha_4 = \frac{2i(A_1|\Omega_2|^2 + 4A_1^2(A_2 + i\nu_{1T})4A_1e^{i\varphi_m}(4A_1A_3 + |\Omega_1|^2 + 4iA_1\nu_{1T}) + 4(A_2 + e^{i\varphi_m}(A_3 + i\nu_{1T}) + i\nu_{1T})\nu_{2T}^2) + 4Q_4e^{\frac{i\varphi_m}{2}}}{(4A_1A_3 + |\Omega_1|^2)|\Omega_2|^2 + 4A_1(A_2|\Omega_1|^2 + 4A_1(A_2A_3 + \nu_{1T}^2)) + 16(A_2A_3 + \nu_{1T}^2)\nu_{2T}^2 - 8|\Omega_1||\Omega_2|\nu_{1T}\nu_{2T}\cos(\varphi_1 - \varphi_2)}.$$

The terms A_{1-4} and Q_{1-4} occurring in α_{1-4} are defined as

$$A_1 = -\left[i\Delta_p + \frac{1}{2}\gamma_{45} + \frac{1}{2}\gamma_{35}\right],$$

$$A_2 = i(\Delta_1 - \Delta_p) - \frac{1}{2}(\gamma_{52} + \gamma_{45} + \gamma_{35} + \gamma_{32}),$$

$$A_3 = i(\Delta_1 - \Delta_p) - \frac{1}{2}(\gamma_{51} + \gamma_{45} + \gamma_{35} + \gamma_{41}),$$

$$Q_1 = 2e^{2i\varphi_1}|\Omega_1||\Omega_2|\nu_{1T} + 2e^{i(2\varphi_2+\varphi_p)}|\Omega_1||\Omega_2|\nu_{1T},$$

$$Q_2 = 4A_1(A_2A_3 + \nu_{1T}^2) + 4i(A_2A_3 + \nu_{1T}^2)\nu_{2T},$$

$$Q_3 = (|\Omega_2|^2 + 4iA_2\nu_{2T} - 4|\Omega_1|e^{i\varphi_2}\nu_{2T}e^{i\varphi_m})$$

and

$$Q_4 = |\Omega_1||\Omega_2|\nu_{2T}\cos(\varphi_1 - \varphi_2 + \frac{\varphi_m}{2}).$$

The matrix form of equation (7) is defined as

$$G = \begin{pmatrix} A_1 & -i\nu_{2T}^* & \frac{i}{2}\Omega_2^* & 0 \\ -i\nu_{2T} & A_2 & 0 & \frac{i}{2}\Omega_1^* \\ \frac{i}{2}\Omega_2 & 0 & A_3 & -i\nu_{1T}^* \\ 0 & \frac{i}{2}\Omega_1 & -i\nu_{1T} & A_4 \end{pmatrix},$$

$$Y = \begin{pmatrix} \frac{i}{2}\Omega_p \\ \frac{i}{2}\Omega_p^*e^{-i\varphi_p} \\ \frac{i}{2}\Omega_m e^{i\varphi_m} \\ \frac{i}{2}\Omega_m \end{pmatrix}, L(t) = \begin{pmatrix} \tilde{\rho}_{35} \\ \tilde{\rho}_{45} \\ \tilde{\rho}_{35} \\ \tilde{\rho}_{15} \end{pmatrix}.$$

References

- [1] Johnson K, Thywissen J, Dekker N, Berggren K, Chu A, Younkin R and Prentiss M 1998 Localization of metastable atom beams with optical standing waves: nanolithography at the Heisenberg limit *Science* **280** 1583–6
- [2] Gorshkov A V, Jiang L, Greiner M, Zoller P and Lukin M D 2008 Coherent quantum optical control with subwavelength resolution *Phys. Rev. Lett.* **100** 093005
- [3] Phillips W D 1998 Laser cooling and trapping of neutral atoms *Rev. Mod. Phys.* **70** 721–41
- [4] Evers J, Qamar S and Zubairy M S 2007 Atom localization and center-of-mass wave-function determination via multiple simultaneous quadrature measurements *Phys. Rev. A* **75** 053809
- [5] Kapale K T, Qamar S and Zubairy M S 2003 Spectroscopic measurement of an atomic wave function *Phys. Rev. A* **67** 023805
- [6] Wu Y, Yang X and Sun C 2000 Systematic method to study the general structure of Bose-Einstein condensates with arbitrary spin *Phys. Rev. A* **62** 063603
- [7] Collins G P 1996 Experimenters produce new Bose-Einstein condensate (s) and possible puzzles for theorists *Phys. Today* **49** 18–21
- [8] Mompert J, Ahufinger V and Birkel G 2009 Coherent patterning of matter waves with subwavelength localization *Phys. Rev. A* **79** 053638
- [9] Storey P, Collett M and Walls D 1992 Measurement-induced diffraction and interference of atoms *Phys. Rev. Lett.* **68** 472–5
- [10] Storey P, Collett M and Walls D 1993 Atomic-position resolution by quadrature-field measurement *Phys. Rev. A* **47** 405–18
- [11] Kunze S, Rempe G and Wilkens M 1994 Atomic-position measurement via internal-state encoding *Europhys. Lett.* **27** 115–21
- [12] Qamar S, Zhu S-Y and Zubairy M S 2000 Atom localization via resonance fluorescence *Phys. Rev. A* **61** 063806
- [13] Liu C, Gong S, Cheng D, Fan X and Xu Z 2006 Atom localization via interference of dark resonances *Phys. Rev. A* **73** 025801

- [14] Herkommer A, Schleich W and Zubairy M 1997 Autler-Townes microscopy on a single atom *J. Mod. Opt.* **44** 2507–13
- [15] Ding C, Li J, Zhan Z and Yang X 2011 Two-dimensional atom localization via spontaneous emission in a coherently driven five-level m-type atomic system *Phys. Rev. A* **83** 063834
- [16] Jiang X, Li J and Sun X 2017 Two-dimensional atom localization based on coherent field controlling in a five-level M-type atomic system *Opt. Express* **25** 31678–87
- [17] Qamar S, Mehmood A and Qamar S 2009 Subwavelength atom localization via coherent manipulation of the Raman gain process *Phys. Rev. A* **79** 033848
- [18] Bharti V and Natarajan V 2015 Study of a four-level system in vee + ladder configuration *Opt. Commun.* **356** 510–4
- [19] Chanu S R, Pandey K and Natarajan V 2012 Conversion between electromagnetically induced transparency and absorption in a three-level lambda system *Europhys. Lett.* **98** 44009
- [20] Khan S, Kumar M P, Bharti V and Natarajan V 2017 Coherent population trapping (CPT) versus electromagnetically induced transparency (EIT) *Eur. Phys. J. D* **71** 38
- [21] Arimondo E 1996 V coherent population trapping in laser spectroscopy *Prog. Opt.* **35** 257–354
- [22] Idrees M, Kalsoom H, Bacha B A, Ullah A and Wang L-G 2020 Continuum and undefined hole burning regions via pulse propagation in a four-level Doppler broadened atomic system *Eur. Phys. J. Plus* **135** 698
- [23] Bharti V and Natarajan V 2017 Sub- and super-luminal light propagation using a Rydberg state *Opt. Commun.* **392** 180–4
- [24] Hau L V, Harris S E, Dutton Z and Behroozi C H 1999 Light speed reduction to 17 metres per second in an ultracold atomic gas *Nature* **397** 594–8
- [25] Mirza A B and Singh S 2017 Subluminal and superluminal light propagation via electromagnetically induced transparency in radiatively and inhomogeneously broadened media *J. Mod. Opt.* **64** 716–24
- [26] Idrees M, Kalsoom H, Bacha B A, Ullah A and Wang L-G 2020 Continuum and undefined hole burning regions via pulse propagation in a four-level Doppler broadened atomic system *Eur. Phys. J. Plus* **135** 698
- [27] Schmidt H and Imamoglu A 1996 Giant Kerr nonlinearities obtained by electromagnetically induced transparency *Opt. Lett.* **21** 1936–8
- [28] Bacha B A and Abdul Jabbar M S 2018 The event cloaking from a birefringent medium via Kerr nonlinearity *J. Optics* **20** 095703
- [29] Lugiato L A 1984 II theory of optical bistability *Prog. Opt.* **21** 69–216
- [30] Bonifacio R and Lugiato L A 1982 Theory of optical bistability *Dissipative Systems in Quantum Optics* (Berlin: Springer) pp 61–92
- [31] Liu Z-Y, Xiao J-T, Lin J-K, Wu J-J, Juo J-Y, Cheng C-Y and Chen Y-F 2017 High-efficiency backward four-wave mixing by quantum interference *Sci. Rep.* **7** 15796
- [32] Ferraz J, Felinto D, Acioli L and Vianna S 2005 Quantum interference in atomic vapor observed by four-wave mixing with incoherent light *Opt. Lett.* **30** 1876–8
- [33] Fleischhauer M, Imamoglu A and Marangos J P 2005 Electromagnetically induced transparency: optics in coherent media *Rev. Mod. Phys.* **77** 633–73
- [34] Alzetta G 1997 Induced transparency *Phys. Today* **50** 36
- [35] Li H, Zhang H, Sun H, Hu X, Sun D and Li X 2017 Multiple spontaneously generated coherence and phase control of optical bistability and multistability in a tripod four-level atomic medium *Appl. Opt.* **56** 4995–5002
- [36] Hamed H R, Sahrai M, Khoshshima H and Juzeliunas G 2017 Optical bistability forming due to a Rydberg state *J. Opt. Soc. Am. B* **34** 1923–9
- [37] Hamed H and Juzeliunas G 2016 Phase-sensitive atom localization for closed-loop quantum systems *Phys. Rev. A* **94** 013842
- [38] Ding C, Li J, Yang X, Zhang D and Xiong H 2011 Proposal for efficient two-dimensional atom localization using probe absorption in a microwave-driven four-level atomic system *Phys. Rev. A* **84** 043840
- [39] Ivanov V S, Rozhdestvensky Y V and Suominen K-A 2014 Three-dimensional atom localization by laser fields in a four-level tripod system *Phys. Rev. A* **90** 063802
- [40] Zhu Z, Yang W-X, Xie X-T, Liu S, Liu S and Lee R-K 2016 Three-dimensional atom localization from spatial interference in a double two-level atomic system *Phys. Rev. A* **94** 013826
- [41] Ivanov V and Rozhdestvensky Y 2010 Two-dimensional atom localization in a four-level tripod system in laser fields *Phys. Rev. A* **81** 033809
- [42] Rahmatullah and Qamar S 2013 Two-dimensional atom localization via probe-absorption spectrum *Phys. Rev. A* **88** 013846
- [43] Zhu Z, Yang W-X, Chen A-X, Liu S and Lee R-K 2015 Two-dimensional atom localization via phase-sensitive absorption-gain spectra in five-level hyper inverted-Y atomic systems *J. Opt. Soc. Am. B* **32** 1070–7
- [44] Wang Z, Cao D and Yu B 2016 Three-dimensional atom localization via electromagnetically induced transparency in a three-level atomic system *Appl. Opt.* **55** 3582–8
- [45] Mao Y and Wu J 2017 High-precision three-dimensional atom localization in a microwave-driven atomic system *J. Opt. Soc. Am. B* **34** 1070–4
- [46] Qi Y, Zhou F, Huang T, Niu Y and Gong S 2012 Three-dimensional atom localization in a five-level M-type atomic system *J. Mod. Opt.* **59** 1092–9
- [47] Bacha B A, Khan T, Khan N, Ullah S A, Jabar A and Rehman A U 2018 The hybrid mode propagation of surface plasmon polaritons at the interface of graphene and a chiral medium *Eur. Phys. J. Plus* **133** 509
- [48] Paspalakis E and Knight P 2001 Localizing an atom via quantum interference *Phys. Rev. A* **63** 065802
- [49] Paspalakis E, Terzis A and Knight P 2005 Quantum interference induced sub-wavelength atomic localization *J. Mod. Opt.* **52** 1685–94
- [50] Idrees M, Bacha B A, Javed M and Ullah S A 2017 Precise position measurement of an atom using superposition of two standing wave fields *Laser Phys.* **27** 045202
- [51] Shah S A, Ullah S, Idrees M, Bacha B A, Javed M and Ullah S A 2019 Surface plasmon induced atom localization in a tripod-type four level atomic system *Phys. Scr.* **94** 035401
- [52] Jabar M S A, Bacha B A, Jalaluddin M and Ahmad I 2015 Atom microscopy via dual resonant superposition *Commun. Theor. Phys.* **64** 741
- [53] Wang Z, Wu X, Lu L and Yu B 2014 High-efficiency one-dimensional atom localization via two parallel standing-wave fields *Laser Phys.* **24** 105501
- [54] Kapale K T and Zubairy M S 2006 Subwavelength atom localization via amplitude and phase control of the absorption spectrum. II *Phys. Rev. A* **73** 023813
- [55] Sahrai M, Tajalli H, Kapale K T and Zubairy M S 2005 Subwavelength atom localization via amplitude and phase control of the absorption spectrum *Phys. Rev. A* **72** 013820
- [56] Xu J and Hu X-M 2007 Sub-half-wavelength localization of an atom via trichromatic phase control *J. Phys. B* **40** 1451–9
- [57] Ali K, Ullah M, Bacha B A and Jabar A 2019 Complex conductivity-dependent two-dimensional atom microscopy *Eur. Phys. J. Plus* **134** 618
- [58] Ding C, Li J, Yang X, Zhan Z and Liu J-B 2011 Two-dimensional atom localization via a coherence-controlled absorption spectrum in an n-tripod-type five-level atomic system *J. Phys. B* **44** 145501

- [59] Wan R-G, Kou J, Jiang L, Jiang Y and Gao J-Y 2011 Two-dimensional atom localization via controlled spontaneous emission from a driven tripod system *J. Opt. Soc. Am. B* **28** 10–7
- [60] Wan R-G, Kou J, Jiang L, Jiang Y and Gao J-Y 2011 Twodimensional atom localization via quantum interference in a coherently driven inverted-y system *Opt. Commun.* **284** 985–90
- [61] Wan R-G, Kou J, Jiang L, Jiang Y and Gao J-Y 2011 Twodimensional atom localization via interacting double-dark resonances *J. Opt. Soc. Am. B* **28** 622–8
- [62] Idrees M, Ullah1 M, Bacha B A, Ullah A and Wang L-G 2020 High-resolution two-dimensional atomic microscopy in a tripod-type four-level atomic medium via standing wave fields *Laser Phys.* **30** 115402
- [63] Kwon D H, Werner P L and Werner D H 2008 Optical planar chiral metamaterial designs for strong circular dichroism and polarization rotation *Opt. Exp.* **16** 11802–7
- [64] Wang B B 1999 Measurement of circular and linear birefringence in chiral media and optical materials using the photoelastic modulator *Proc. SPIE* **3535** 294–302
- [65] Narushima T and Okamoto H 2016 Circular dichroism microscopy free from commingling linear dichroism via discretely modulated circular polarization *Sci. Rep.* **6** 35731
- [66] Wang B, Sparks W B, Germer T A and Leadbetter A 2009 A spectroscopic polarimeter for detecting chiral signatures in astrobiological samples *Proc. SPIE* **7441** 744108
- [67] Silverman M P and Sohn R B 1986 Effects of circular birefringence on light propagation and reflection *Am. J. Phy.* **54** 69–76
- [68] Kang L, Hao Z, Taiwei J, Douglas Y and Werner H 2015 Handedness dependent electromagnetically induced transparency in hybrid chiral metamaterials *Sci. Rep.* **5** 12224
- [69] Iqbal H, Idrees M, Javed M, Bacha B A, Khan S and Ullah S A 2017 Goos hanchen shift from cold and hot atomic media using kerr nonlinearity *J. Russ. Laser Res.* **38** 426–36
- [70] Khan M I, Idrees M, Bacha B A, Khan H, Ullah A and Haneef M 2020 Optical soliton through induced cesium doppler broadening medium *Phys. Scr.* **95** 085102